

Rajiv Bharadwaj<sup>1</sup>  
Juan G. Santiago<sup>2</sup>  
Bijan Mohammad<sup>3</sup>

## Design and optimization of on-chip capillary electrophoresis

<sup>1</sup>Chemical Engineering  
Department  
<sup>2</sup>Mechanical Engineering  
Department, Stanford  
University, Stanford,  
CA, USA  
<sup>3</sup>Laboratories of Mathematics  
CC51,  
University of Montpellier II,  
Montpellier, France

We present a systematic, experimentally validated method of designing electrokinetic injections for on-chip capillary electrophoresis applications. This method can be used to predict point-wise and charge-coupled device (CCD)-imaged electropherograms using estimates of species mobilities, diffusivities and initial sample plug parameters. A simple Taylor dispersion model is used to characterize electrophoretic separations in terms of resolution and signal-to-noise ratio (SNR). Detection convolutions using Gaussian and Boxcar detector response functions are used to relate optimal conditions for resolution and signal as a function of relevant system parameters including electroosmotic mobility, sample injection length, detector length scale, and the length-to-detector. Analytical solutions show a tradeoff between signal-to-noise ratio and resolution with respect to dimensionless injection width and length to the detector. In contrast, there is no tradeoff with respect to the Peclet number as increases in Peclet number favor both SNR and separation resolution ( $R$ ). We validate our model with quantitative epifluorescence visualizations of electrophoretic separation experiments in a simple cross channel microchip. For the pure advection regime of dispersion, we use numerical simulations of the transient convective diffusion processes associated with electrokinetics together with an optimization algorithm to design a voltage control scheme which produces an injection plug that has minimal advective dispersion. We also validate this optimal injection scheme using fluorescence visualizations. These validations show that optimized voltage scheme produces injections with a standard deviation less than one-fifth of the width of the microchannel.

**Keywords:** Electrokinetic injection / Microchip / One-chip capillary electrophoresis EL 5080

### 1 Introduction

#### 1.1 General aspects

On-chip electrophoresis devices offer key advantages over more traditional capillary systems including higher resolution, low sample volume requirements, shorter analysis times and parallel architecture [1, 2]. As device dimensions decrease, system throughputs increase, and automation schemes become more complex, quantitative methods of characterizing and designing electrophoretic separations are required. In particular, traditional performance criteria based on plate height models [3], as will be discussed below, do not fully describe the efficiency of a separation. One approach to analyzing electrophoretic processes is to perform fully coupled numerical simulations of the partial differential equation governing the electromigration-convective-diffusion problem of electro-

kinetics. Bier *et al.* [4] developed a fairly comprehensive electrophoresis separation system for capillary based separation systems. Recently, Ermakov *et al.* [5] and Patankar and Hu [6] developed computational tools to analyze the temporal and spatial distribution of ions in microchip-based electrokinetic separation devices. Such simulations can provide accurate and detailed information concerning the dynamics of particular processes, but lack a general insight into the problem and do not provide a broadly applicable, straightforward method of designing separation systems

In this paper we propose the use of a signal-to-noise ratio (SNR) model and a nondimensional separation resolution ( $R$ ) as the criteria for characterizing the efficiency of separations and for systematic design of separation experiments. Use of SNR as a separation efficiency criterion is especially appropriate for microscale devices where small optical path lengths lead to decrease in the sensitivity of detectors and separations can often be SNR limited. To develop a simple design methodology applicable across a wide range of Peclet numbers (see next section), we use an analytical model based on Taylor dispersion equation for sample concentration distribution and various detector response functions. Also, for the case of very high advective-to-diffusive flux ratios (*i.e.*, high Pec-

---

**Correspondence:** Rajiv Bharadwaj, Mechanical Engineering Department, Stanford University, Building 500, Room 500Y, Stanford, CA 94305, USA  
**E-mail:** rajivb@stanford.edu  
**Fax:** +650-723-7657

**Abbreviation:** SNR, signal-to-noise ratio

let number separations) we present a three-step injection scheme which achieves an injection sample plug of minimal advective dispersion and can be used to achieve very short sample plugs using a simple cross microchip.

## 1.2 Theory

In this section, we present a brief discussion of the merits and limitations of several criteria used for characterizing electrophoretic separations. We then use the convection-diffusion equation to describe the concentration distribution of sample ions for various dispersion regimes relevant to on-chip electrophoresis systems.

### 1.2.1 Performance indices

A schematic of a simple microchip separation system is shown in Fig. 1. The figure summarizes relevant length scales of the problem including the channel hydraulic diameter,  $w$ , the separation length,  $L_d$ , the characteristic analyte band width,  $\sigma$ , and the shortest separation distance between sample peaks,  $\Delta L$ . The analyte band width,  $\sigma$ , here is defined as the standard deviation of the width-integrated concentration distribution of the analyte band. We consider both cross-injections and double-T injection systems for finite and zero values of the stagger length,  $h$ . The stagger is approximately the length of the injection plug.  $E$  is the applied electric field. Frequently used separation indices include separation resolution, peak capacity, plate height and number of theoretical plates. This section presents a short summary of these indices as an explanation of the figures of merit chosen in this paper.

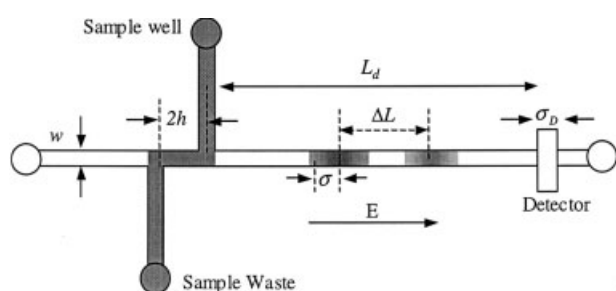


**Figure 1.** Schematic of a microchip-based electrophoretic separations system. Important length scales to characterize separation performance include the length-to-detector, sample injection width, detector width, sample variance, and distance between the two most closely spaced analyte peaks. Typically, electroosmotic flow is higher than the analyte mobilities and a single detector downstream can be used to detect positive, negative, and neutral analytes.

Resolution can be defined as the ratio of the distance between sample peaks and the standard deviation of the sample zones (see Fig. 2):

$$R = \Delta L / \sigma \quad (1)$$

For a separation system with three or more sample ions, an overall separation resolution can be defined as the resolution achieved for the two analytes which are most difficult to separate (small mobility difference and/or large diffusion coefficient). For a conservative estimate of the resolution, the larger of the two analyte band standard deviations should be used [7]. This definition of the resolution describes the degree to which the two most challenging analyte bands have been distinguished and is probably the most important factor in characterizing the efficiency of a separation (particularly in systems not limited by signal-to-noise (SNR)). Various sources of dispersion (a.k.a., band broadening) of analyte bands include molecular diffusion, dispersion due to pressure gradients, Joule-heating-induced analyte dispersion, initial injection plug variance, and detector variance [8].

A second important separation criterion is the number of sample zones per unit length of the separation channel. This is referred to as the peak capacity of the system [3] and can be expressed as

$$n_c = L_o / 4\sigma R \quad (2)$$

where  $L_o$  is the length of the separation column which contains  $n_c$  analyte band peaks. This parameter is particularly useful for techniques where a spatial, full-field detection (*i.e.*, a spatial concentration distribution) of many analyte bands is performed as in the read out of a two-dimensional electrophoresis/isoelectric focusing gel slabs [9]. For such detections, peak capacity is proportional to the number of analyte bands that can be resolved simultaneously in the available space of length scale  $L_o$ . Peak capacity is less useful in systems where a transient signal is produced from a point-wise detection of bands as in the case of many on-chip electrophoresis systems. Consider that, in such a case, using  $L_d$  in place of  $L_o$  is not appropriate since the length  $L_d$  does not bound a region of sample peaks as in full-field detection. For example, replacing using  $L_d$  in place of  $L_o$  in Eq. (2) yields a term equal to  $L_d / 4\Delta L$  which is not descriptive of the number of analyte bands discerned by a point-wise temporal detection. In such a case, the value of  $L_d / 4\Delta L$  is not at all indicative of whether a successful separation (with sufficient resolution) has been made or how many species can be detected.

Plate models for electrophoretic separations are used very frequently for overall system-to-system comparisons of separation efficiency. Plate models have historically

been used for describing stage-wise distillation columns [10]. Two indices relevant to the plate model are plate height and the number of theoretical plates. Plate height,  $H$ , is defined as

$$H = \sigma^2/L_d \quad (3)$$

Although there are no physical plates in electrophoresis,  $H$ , characterizes the dispersion incurred by the sample plug per unit separation length. A derivative term,  $NTP$ , called the number of theoretical plates, can be defined

$$NTP = (L_d/\sigma)^2 \quad (4)$$

The “efficiency” of separation is typically said to be higher for systems with higher plate number.

Despite the widespread use of the plate model for characterizing electrophoretic separations, the model has important fundamental limitations in describing the quality of a separation. Plate height is not a useful parameter because it does not communicate whether a successful separation has been achieved and detected. Plate height is a dimensional parameter and hence ambiguous for comparing the relative performance of two different systems. That is, the plate height of system A, which cannot resolve a set of analytes can be smaller than that of system B; while system B actually resolves all analytes with higher  $SNR$ . Combining Eqs. (1) and (3) to express plate height as  $(\Delta L)^2/(R^2 L_d)$ , we see how plate height can be arbitrarily small or large for a given nondimensional resolution  $R$  and various values of the ratio  $(\Delta L)^2/L_d$ . In turn,  $(\Delta L)^2/L_d$  depends on the mobility of the separation channel walls and the mobility of analyte bands. The definition of “high plate number” to quantify the performance of a separation is also arbitrary and thus limits the usefulness of  $N$  as a figure of merit. The application of plate heights to CE is typically attributed to Giddings [11] who qualifies the use of plate models as follows: “The concept of theoretical plates evolved from studies of distillation and countercurrent distribution, where distinct stages frequently exist . . . Plate models, however, are neither very appropriate nor very useful in describing the continuous transport processes of chromatography, field-flow fractionation, electrophoresis, sedimentation, and related zonal methods.”

Giddings then argues that, although plate height models “yield little of value” in zonal methods, they do obey the commonly observed scaling of dispersion which describes the variance of an analyte band as  $\sigma^2 = HL$ . He therefore advocates their use in unifying the comparison of widely different separation methods such as CE and chromatography. However, this type of scaling in zonal methods is simply a result of the dynamics of diffusive phenomena (where diffusion length scales as the

square root of travel time) and can be fairly generally incorporated into descriptions of separations using simple convective diffusion models as we do in this paper. Plate height models therefore are only artificially introduced into analyses of separation resolution and “efficiency.” By itself, plate height is not descriptive of the efficacy of a separation of a zonal method.

In this paper, we present an unambiguous description of separation efficiency using  $SNR$  and a simple nondimensional resolution parameter. This model is based on two key principles governing the success of an electrophoretic separation: (i) separation resolution, defined above, which refers directly to the ability to discriminate the two most closely placed analyte peaks and (ii) the  $SNR$  which directly describes our ability to discern the signal produced by the analytes from background noise. Adequate  $R$  and  $SNR$  together completely determine the efficacy of a given separation. We define  $SNR$  as the ratio of a signal peak height relative to a mean noise level to the standard deviation of background signal, as depicted in Fig. 2.

$$SNR = I_o/N_{RMS} \quad (5)$$

This definition of  $SNR$  can be interpreted as a probabilistic statement about the certainty with which a signal peak can be distinguished from random noise. The success of an electrophoretic separation can be nearly completely

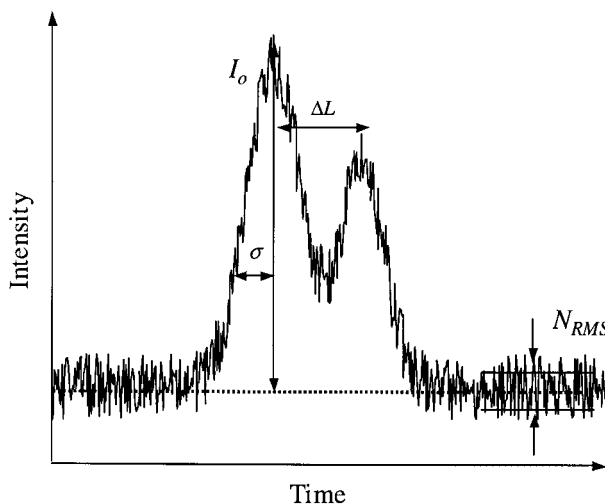


**Figure 2.** Schematic representation of the detector output for defining separation resolution and signal-to-noise ratio. This simulated signal was specified as the sum of two Gaussian distributions in time in a normally distributed background white noise. We define the  $SNR$  as the ratio of the peak intensity to a characteristic noise width. The peak is defined as the signal in excess of the mean value of local noise. The noise width can be defined as twice the standard deviation of the noise amplitude.

described by satisfactory values of  $SNR$  and  $R$ . In this paper, we will describe a successful separation using the following inequalities:

$$R \geq R_c \quad (6)$$

$$SNR \geq SNR_c$$

where  $R_c$  and  $SNR_c$  are user-defined critical resolution and signal-to-noise ratio values that characterize a successful separation and detection. For example for a typical successful separation experiment we will here assume that  $R \geq 2$  and  $SNR \geq 3$ . In contrast with the plate model, this  $SNR$ - $R$  model is based on dimensionless parameters that make system-to-system performance comparisons of electrophoretic separations unambiguous. Also, as we show later, these parameters can be easily related to the temporal and spatial development of analyte bands thereby capturing the continuous electrophoretic process more accurately.

### 1.2.2 Regimes of dispersion of analyte bands

To design separation experiments in a systematic manner, we need definitions of  $SNR$  and  $R$  in terms of the concentration distributions of analyte ions. Three important regimes for sample dispersion can be identified [12] based on a Peclet number,  $Pe$ , based on a dispersive velocity scale  $U_d$  and the ratio  $L_d/w$ . The Peclet number is defined as the ratio of advective-to-diffusive flux of analyte ions:

$$Pe = \frac{U_d w}{D} \quad (7)$$

where  $D$ ,  $U_d$  and  $w$ , are diffusion coefficient, bulk average velocity scale (for the analyte), and the width of the channel (or a characteristic length scale), respectively. Note that if the bulk velocity is due to ideal plug-like ( $U_d = 0$ ) electroosmotic flow [12], then the only mechanism for dispersion is molecular diffusion. Three regimes are discussed below.

#### 1.2.2.1 Axial diffusion limit

$Pe \ll 1$ : In this regime, band broadening is dominated by molecular diffusion. The sample plug variance due to dispersion is simply

$$\sigma^2 = 2Dt \quad (8)$$

where  $D$  is the molecular diffusion coefficient.

#### 1.2.2.2 Taylor-Aris limit

In this regime, both advection and transverse diffusion are important. This regime has been described by Aris [13] as a generalization of Taylor dispersion model [14]. In the

Taylor-Aris regime, the dispersion is modeled using an effective diffusion coefficient. For example, for simple pressure driven flow in a cylindrical tube effective diffusion coefficient is of the form [12]:

$$D_{\text{eff}} = D \left( 1 + \frac{w^2 U_d^2}{48D^2} \right) \quad (9)$$

where  $U_d$  is the area-averaged (*i.e.*, bulk) pressure driven flow velocity:

$$U_d = -\frac{w}{8\mu} \frac{dP}{dx} \quad (10)$$

Similar relations can be derived for noncircular channel geometries [15]. In this paper, we will apply this Taylor-Aris model to a CE separation. The general area-averaged velocity of the analyte,  $U$ , can be expressed as

$$U = U_d + U_{\text{eof}} + U_{\text{ep}} = E(\mu_{\text{eof}} + \mu_{\text{ep}}) + U_d = E\mu_{\text{eff}} + U_d \quad (11)$$

where  $U_{\text{eof}}$  and  $U_{\text{ep}}$  are the (plug-like) electroosmotic and electrophoretic components of the analyte velocity, respectively. For such a system, the condition for which the Taylor-Aris limit is applicable can be expressed as

$$Pe \ll \frac{L_{\text{eff}}}{w} \quad (12)$$

where  $L_{\text{eff}}$  is the displacement due to  $U_d$  in a reference frame moving at a velocity ( $U_{\text{eof}} + U_{\text{ep}}$ ), so that

$$L_{\text{eff}} = \frac{U_d}{U_d + U_{\text{ep}} + U_{\text{eof}}} L_d \quad (13)$$

Various band-broadening mechanisms such as induced pressure gradients due to zeta potential variations [16, 17] and Joule heating [18] can also be analyzed using the Taylor-Aris dispersion model presented here. Such analysis would involve calculation of the new effective diffusivity and the new associated “long time” criteria for Taylor-Aris-like dispersion. Below, we will use  $D_{\text{eff}}$ , to denote the effective diffusivity for arbitrary channel geometry of interest and for arbitrary band broadening mechanism(s) governing dispersion.

#### 1.2.2.3 Pure advection limit

$Pe \gg L/w$ : This regime is characterized by negligible dispersion of the sample plug due to molecular diffusion. For electroosmotic flows with negligible velocity gradients, the initial injection sample variance dominates the overall variance of analyte bands. Consequently, in this regime a fine control of the injection plug shape and size will have the most important effect on separation resolution.

### 1.2.3 Analyte concentration distribution

For the axial diffusion limit and Taylor-Aris limit the spatial and temporal, cross-section averaged concentration distribution for the analytes can be described by the Taylor dispersion equation [12] with appropriately defined effective diffusion coefficient:

$$\frac{\partial C}{\partial t} + U \frac{\partial C}{\partial x} = D_{\text{eff}} \frac{\partial^2 C}{\partial x^2} \quad (14)$$

This equation describes the temporal and spatial development of the analyte band distribution. Analytical solutions for the development of analyte bands can be derived for realistic injection profiles (e.g., a Gaussian sample zone produced by a simple cross microchip or a nearly boxcar-shaped profile produced by a double T microchip injection).

#### 1.2.3.1 Gaussian injection

An injection plug with an approximately Gaussian axial intensity profile for the cross-sectional area averaged intensity  $C$  can be expressed as:

$$C(x, 0) = \frac{C_0}{\sigma_0 \sqrt{2\pi}} \exp\left(-\frac{x^2}{2\sigma_0^2}\right) \quad (15)$$

where  $\sigma_0$  is the initial injection standard deviation.

For this initial condition, solution of the Taylor dispersion Eq. (14) is simply

$$C(x, t) = \frac{C_0}{\bar{\sigma} \sqrt{2\pi}} \exp\left(-\frac{(x - Ut)^2}{2\bar{\sigma}^2}\right) \quad (16)$$

where,  $\bar{\sigma}^2 = \sigma_0^2 + 2D_{\text{eff}}t$ .

#### 1.2.3.2 Boxcar injection

A large injection plug produced by a double-T type injection geometry can be approximated as a boxcar function described as

$$C(x, 0) = \begin{cases} C_0 & -h \leq x \leq h \\ 0 & \text{otherwise} \end{cases} \quad (17)$$

For the this boxcar shape the solution of the Taylor dispersion equation is:

$$C(x, t) = \frac{C_0}{2} \left[ \text{erf}\left(\frac{h - x + Ut}{\sigma\sqrt{2}}\right) + \text{erf}\left(\frac{h + x - Ut}{\sigma\sqrt{2}}\right) \right] \quad (18)$$

where  $\sigma^2 = 2D_{\text{eff}}t$ .

In the next section we use these simple, well-known relations to develop analytical models for the time-varying signal generated by an on-column detector.

## 2 Methods

### 2.1 Analytical models

To calculate the signal generated by a detection system,  $I$ , we look at two representative detection modes: CCD arrays and point-wise detection systems. CCD array detectors simultaneously provide high resolution temporal as well as spatial information about concentration distributions in electrophoretic separation experiments. This is a major advantage over single point detectors where only temporal information can be acquired. CCD arrays are especially useful when used as a full-field detection system because detailed information about the dynamics of the process can be recorded. Single point detectors are commonly used to measure the concentration profiles as a function of time at a single location, and are typically simpler to set up and cheaper than CCD arrays. Single point detectors include laser-induced fluorescence (LIF) detectors, ultraviolet radiation absorption detectors, and conductivity detector [18].

#### 2.1.1 CCD array detectors

In most applications, CCD arrays provide two-dimensional line-of-sight integrated information about the concentration distribution. The detection process can be described as

$$I(x, y, t) = D_0 \int C(x, y, z, t) dz \quad (19)$$

Here,  $I$  is the two-dimensional intensity as recorded by the camera,  $D_0$  is a detector response parameter which converts the sample concentration to intensity values. To derive an analytical one-dimensional model for detector output we consider a channel width averaged intensity distribution

$$\begin{aligned} \bar{I}(x, t) &= \int I(x, y, t) dy = \\ &= \frac{D_0}{w} \iint C(x, y, z, t) dy dz = D_c C'(x, t) \end{aligned} \quad (20)$$

where  $C'(x, t)$  signifies an average both over the depth of the channel and over the channel width. A general analytical expression for  $C'(x, t)$  is difficult. However, if the concentration variation over the depth of the channel is not significant, then we can approximate the three dimensional concentration distribution as a two-dimensional distribution or

$$C(x, y, z, t) \approx C(x, y, t) \quad (21)$$

This assumption is good for shallow channels where diffusion quickly homogenizes the concentration field in the  $z$ -direction. Under this assumption, the results of the Taylor

dispersion equation can be used directly to describe the cross-sectional area averaged intensity profiles. For example, for Gaussian sample injection

$$I_{\text{CCD}}(x, t) = \frac{I_0}{\bar{\sigma}\sqrt{2\pi}} \exp\left(-\frac{(x - Ut)^2}{2\bar{\sigma}^2}\right) \quad (22)$$

where,  $\bar{\sigma}^2 = \sigma_0^2 + 2D_{\text{eff}}t$  and  $I_0 = D_0C_0$ .

## 2.1.2 Single point detectors

The detection process in capillary zone electrophoresis with a point-wise detector can be modeled as convolution of the concentration distribution with the detector response function. We model the single point detectors in two ways, as a Gaussian response function and a Boxcar response function.

### 2.1.2.1 Gaussian aperture model

The detector response,  $D(x)$ , for a point-detection system with a Gaussian spatial distribution can be represented as

$$D(x) = \frac{D_0}{\sqrt{2\pi}\sigma_D} \exp\left(-\frac{(x - L_d)^2}{2\sigma_D^2}\right) \quad (23)$$

where  $L_d$  is the length to the detector,  $\sigma_D^2$  is the variance associated with the detection system and  $D_0$  is the characteristic response of the detector. This type of detector response would be expected from a LIF detector, which applies a laser beam with a diameter that scales as  $\sigma_d$  and a photomultiplier tube (PMT) and lens system which captures intensities throughout this laser-illuminated region. The signal generated is

$$I(t) = \int_{-\infty}^{\infty} D(x)C(Ut - x, t)dx \quad (24)$$

Evaluation of Eq. (24) using Eq. (16) to describe a Gaussian injection profile and Eq. (23) to describe the detector response, results in

$$I(t) = \frac{I_0}{\bar{\sigma}\sqrt{2\pi}} \exp\left(-\frac{(L_d - Ut)^2}{2\bar{\sigma}^2}\right) \quad (25)$$

where  $I_0 = D_0C_0$

$$\bar{\sigma}^2 = \sigma_0^2 + \sigma_D^2 + 2D_{\text{eff}}t$$

Note how the signal peak widths depend on initial sample plug length, detector width, and the elution time  $t$ .

Gaussian aperture detection of a boxcar injection: Evaluation of Eq. (24) using Eq. (18) to describe a simple boxcar injection profile and Eq. (23) to describe the detector response, results in

$$I(t) = \frac{I_0}{2} \left( \operatorname{erf}\left(\frac{h - L_d + Ut}{\sqrt{2}\bar{\sigma}}\right) + \operatorname{erf}\left(\frac{h + L_d - Ut}{\sqrt{2}\bar{\sigma}}\right) \right) \quad (26)$$

where  $I_0 = D_0C_0$

$$\bar{\sigma}^2 = \sigma_0^2 + 2D_{\text{eff}}t$$

We see that the concentration profile depends on the initial sample plug length, detector width, length-to-detector and the elution time  $t$ .

### 2.1.2.2 Boxcar aperture model

Next, we consider a simple boxcar aperture model for the detector which can be represented as

$$D(x) = \begin{cases} D_0, & x \in [L_d - \delta, L_d + \delta] \\ 0, & \text{otherwise} \end{cases} \quad (27)$$

This type of detector response would be consistent with, for example, an LIF set up where a laser beam with diameter significantly larger than  $D_0$  is imaged with an apertured field of view with an axial length equal to  $\delta$ . Other applications of this formulation can be found in UV absorption detectors and potentiometric detectors. Convolution of the concentration field with the detector response function gives

$$I(t) = \int_{L_d - \delta}^{L_d + \delta} D_0C(Ut - x, t)dx \quad (28)$$

For both Gaussian and boxcar injections, this integral can be calculated analytically to derive  $I(t)$ , the results are presented in Appendix A.

### 2.1.3 Nondimensionalization

To isolate important system parameters, we can nondimensionalize the detector outputs derived in the previous sections. Without any loss of generality we nondimensionalize Eq. (26) using detector standard deviation,  $\sigma_d$  as the characteristic length scale,  $L_d/U$  as the time scale, and  $I_0$  as the signal intensity scale

$$I'(t') = \frac{1}{2} \left( \operatorname{erf}\left(\frac{h' - L'_d + L'_d t'}{\sqrt{2}(1 + 2(Pe_{\sigma_0})^{-1}L'_d t')}}\right) + \operatorname{erf}\left(\frac{h' + L'_d - L'_d t'}{\sqrt{2}(1 + 2(Pe_{\sigma_0})^{-1}L'_d t')}}\right) \right) \quad (29)$$

Primed quantities are dimensionless. Three important dimensionless parameters governing the detector output are:  $L'_d$ , the ratio of the length to the detector and the detector width,  $h'$ , the ratio of the initial sample plug

length and the detector width, and  $Pe_{\sigma_D} = \sigma_D U / D_{\text{eff}}$ , the ratio of time to diffuse through the width of the detector to the time to advect across the detector.

## 2.2 Application of the model

In this section, we use the models developed above to express  $SNR$  and  $R$  in terms of system parameters and to develop guidelines for the design of separation experiments. An important parameter of interest is the time variance of the temporal signal intensity for a single analyte which can be expressed as

$$\sigma^2 = \frac{\int (t - \mu)^2 I(t) dt}{\int I(t) dt} \quad (30)$$

The analytical evaluation of this integral is tedious because  $I(t)$  is a complex function of time. However, a simplifying assumption of “frozen analyte band” can be made when the analyte bands do not diffuse (or separate from each other) significantly as they pass through the detector. This assumption is valid for two different regimes. First, the sample does not diffuse significantly when either the analyte dispersion falls in the purely advective regime in a plug like flow so that

$$Pe_{\sigma_D} \gg L'_d \quad (31)$$

Second, when  $Pe_{\sigma_D} < L'_d$  and there is significant dispersion in the separation, but the band broadening is negligible during the time of travel across the detector window as compared to the overall sample variance due to dispersion, or

$$2D_{\text{eff}} \left( \frac{\sigma_D}{U} \right) \ll 2D_{\text{eff}} \left( \frac{L'_d}{U} \right) \quad (32)$$

or  $L'_d \gg 1$

For typical system parameters in on-chip electrophoretic separations, the latter condition is valid. For example, for  $L_d = 0.1$  m,  $\sigma_D = 10$   $\mu\text{m}$ ,  $U = 0.001$  m/s,  $D = 1 \times 10^{-10}$  m<sup>2</sup>/s,  $h = 50$   $\mu\text{m}$ ;  $Pe_{\sigma_D} = 100$ ,  $L'_d = 10\,000$ .

Figure 3 presents results from the analytical model developed here. Curve a shows a diffused boxcar analyte band profile for a high Peclet number case. Curve b shows the effect of increased dispersion (low Peclet number limit), here diffusion of the initially uniform distribution results in a symmetric analyte band, which is approximately Gaussian with a lower peak height and larger variance. Curve c shows the case where the “frozen” assumption is violated and an asymmetric tailing intensity profile is observed. This asymmetry results from the fact that conditions described by Eqs. (31) and (32) are not met and the analyte band disperses significantly as it passes through the detection region. The development of the band during

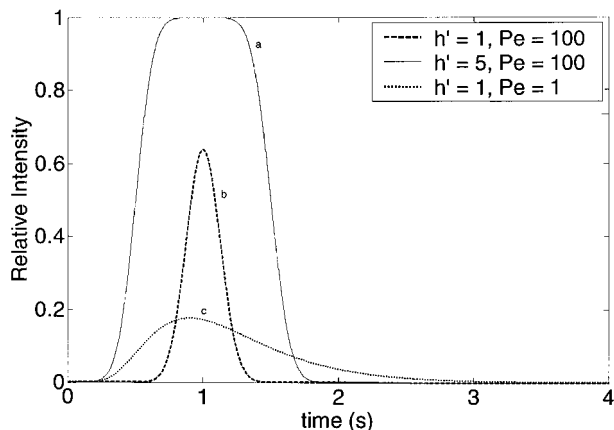


**Figure 3.** Predicted signal for an analyte band detected with a point-wise detector with a Gaussian response as calculated using Eq. (29). All three curves are calculated for  $L'_d = 10$ . Curve a represents a high Peclet number, high sample injection length profile showing a plateau in concentration profile. Curve b is a high Peclet number case with a low injection length, which leads to a transition from a plateau profile to a Gaussian profile with a lower peak intensity. Curve c is an example of an analyte band detection where the violation of frozen sample plug assumption leads to excessive dispersion and a tailing profile.

detection results in a slow roll-off of the temporal intensity profile as the peak leaves the detection zone. Note that, for this nonfrozen flow condition, the peak is not centered at  $t_d = L_d/U$ . This again is a result of the excessive dispersion of the band as it passes through the detector.

When the frozen plug assumption is not valid, the denominator in Eq. (26) varies strongly with time and evaluation of the variance integral is tedious. However, as described earlier, for most cases of interest the frozen plug assumption is valid and we can assume that

$$\bar{\sigma}^2 \approx \sigma_D^2 + 2D_{\text{eff}} t_d \quad (33)$$

This approximation states that, under the frozen sample plug assumption, the sample plug variance can be assumed to be a constant in time during the detection period and equal to the variance at  $t = t_d$ . Making this frozen-flow assumption, the net variance of the sample plug can be easily calculated by realizing that the integral in Eqs. (24) and (28) are simple convolutions so that the variances can be simply related as

$$\sigma^2 (f \otimes D(x)) = \sigma^2 (f) + \sigma^2 (D(x)) \quad (34)$$

where  $f(x)$  is equal to  $C(x, t_d)$ , and the operator  $\otimes$  indicates a convolution of the form given by Eqs. (24) and (28).

Hence, we can express the variance of the plug during the time of detection for the frozen flow case as,

$$\sigma_{\text{net}}^2 = \frac{h^2}{3} + 2D_{\text{eff}}t_d + \sigma_D^2 = \sigma_{\text{injection}}^2 + \sigma_{\text{Dispersion}}^2 + \sigma_{\text{Detector}}^2 \quad (35)$$

We see that this is the familiar “sum squares” result often applied in the analysis of electropherograms wherein the resulting variance is the sum of the variances due to the individual peak broadening mechanisms.

Having calculated the expression for net variance separation,  $R$  and  $SNR$  can be related to dispersion processes as follows

$$R = \frac{\alpha L'_d}{(1 + \beta) \sqrt{1 + (h^3/3) + 2(Pe_{\sigma_D})^{-1} L'_d}} \quad (36)$$

where  $\alpha$  is a parameter based on the ratio of difference in electrophoretic mobility to an effective mobility scale,  $\alpha = (\Delta\mu)/\mu_{\text{eff}}$  and  $\beta = U_d/E\mu_{\text{eff}}$ . Note that  $\alpha$  is a parameter determined solely by the chemistry of the species to be separated (*i.e.*, not typically a control parameter) while  $\beta$  is a non-dimensional description of the dispersive velocity component which, of course, should always be minimized.

$SNR$  is in general a detector-dependent function that varies with sample concentration, channel geometry, lens collection efficiency, illumination conditions, photo-(or electro)chemical detection phenomena, and noise sources (*e.g.*, background fluorescence sources and preamplifier noise in a photodetector). For separation experiments, a simple way to define  $SNR$  is the ratio of the analyte peak intensity to the mean noise associated with the detection system

$$SNR = \frac{I_0}{N} \operatorname{erf} \left( \frac{h'}{\sqrt{2(1 + 2(Pe_{\sigma_D})^{-1} L'_d)}} \right) \quad (37)$$

where  $N$  represents the noise associated with the detector. In the next section we use these definitions to develop the design methodology for electrophoretic separations. The value of  $I_0/N$  can be measured experimentally for each microchannel and detection system configuration of interest. After an initial estimation of this value and the initial sample plug mean and variance, the model developed here can be used predict a wide range of trends associated with the parameters  $SNR$  and  $R$ .

### 2.3 Design of electrophoretic separations

In a typical separation experiment there are a number of parameters affecting the system performance. These can be broadly categorized as parameters determined by the

chemistry such as mobility of ions, diffusion coefficients, sample concentration and channel mobility; and detector controlled parameters such as width of the detector, sensitivity and noise level; and free parameters such as width of the sample plug, length to the detector and electric field intensity. In general the designer has little control over the first set of these and the second is typically limited by the equipment available. However, the designer can easily manipulate the three independent parameters:  $L_d$ ,  $h$ ,  $E$ , to optimize the performance of simple electrophoretic separations. In the definition of  $R$  and  $SNR$  the three tunable parameters appear in dimensionless parameters as  $L'_d$ ,  $h'$  and  $Pe_{\sigma_D}$ , respectively.

A fourth parameter in the problem is the dispersive term,  $\beta$ , in Eq. (36). In general,  $\beta$  is difficult to predict from system to system and, to simplify the analyses presented below, we will assume that the value of  $\beta$  is negligible. More generalized approaches to the optimization of capillary electrophoretic separations should treat  $\beta$  as a design parameter since, for example, as described in Eq. (10), the magnitude of  $U_d$  for pressure driven flow in a capillary is a function of the characteristic scale of the channel width. As discussed later, dispersion effects other than molecular diffusion were negligible in our electrophoresis experiments.

Figure 4 demonstrates the dependence of  $SNR$  and  $R$  on dimensionless initial sample plug length,  $h'$ . Increasing sample plug length increases the  $SNR$  but reduces the resolution. Larger plug lengths lead to a delay in the transition from a Boxcar to a Gaussian profile of decreasing peak value and hence the signal is higher even at larger times. As expected, large sample injection widths reduce resolution and this is especially critical when the overall

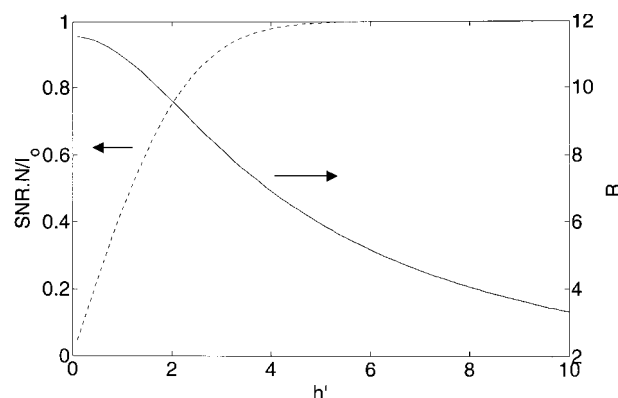


**Figure 4.** Effect of dimensionless sample injection width on  $SNR$  and  $R$  as calculated using Eqs. (36) and (37) respectively. A tradeoff exists between  $SNR$  and  $R$  as the nondimensional sample injection length is increased from 0 to 10. Values of,  $Pe_{\sigma_D} = 100$ ,  $L'_d = 100$ ,  $\beta = 0$  and  $\alpha = 0.2$  were used for both curves. The system-dependent value of  $I_0/N$  is used to normalize  $SNR$ .

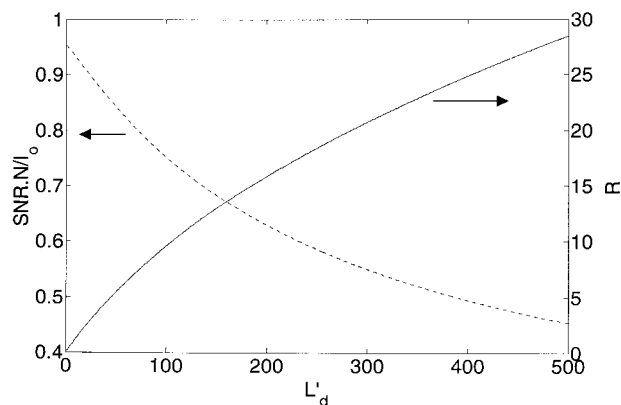


**Figure 5.** Effect of dimensionless length to the detector on *SNR* and *R*. Again, a tradeoff exists between *SNR* and *R* as the nondimensional detector length is increased. For both curves:  $h' = 2$ ,  $Pe_{\sigma_D} = 100$ ,  $\beta = 0$  and  $\alpha = 0.2$ .

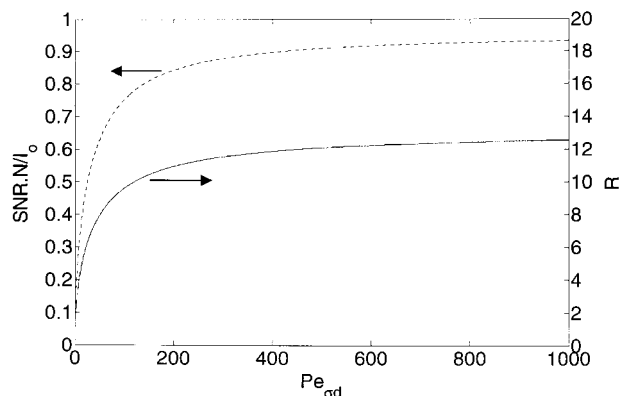


**Figure 6.** Effect of Peclet number on *SNR* and *R*. Increase in Peclet number improves both *SNR* and *R*. For both curves  $h' = 2$ ,  $L'_d = 100$ ,  $\beta = 0$  and  $\alpha = 0.2$ .

sample variance is governed by the initial injection width. There is thus a quantifiable tradeoff between *SNR* and *R* with respect to initial sample plug lengths. Figure 5 again shows a similar quantifiable tradeoff between the dimensionless form of separation length  $L'_d$ . An increase in length to the detector increases the resolution by providing longer times for the two ions to separate, but decreases the *SNR* because the sample plug variance increases with length to the detector. Since signal peaks drop off as the square root of time but separation between bands scales directly with time, longer lengths are always favorable up to the point where *SNR* limits detection. Figure 6 shows that increase in  $Pe_{\sigma_D}$ , improves both the resolution and *SNR*. As shown in the plot, *SNR* and *R* asymptotically approach following values at large  $Pe_{\sigma_D}$

$$R|_{Pe_{\sigma_D} \rightarrow \infty} = \frac{\alpha L'_d}{\sqrt{1 + (h'^2/3)}} \quad (\text{for } \beta = 0) \quad (38)$$

$$SNR|_{Pe_{\sigma_D} \rightarrow \infty} = \frac{l_0}{N} \operatorname{erf}\left(\frac{h'}{\sqrt{2}}\right) \quad (\text{for } \beta = 0)$$

These limits are both associated with the pure advection regime and can be seen as the upper bounds on the maximum realizable resolution and *SNR* for fixed  $h'$ ,  $L'_d$ . In terms of free variables this indicates that the electric field intensity should be as high as admissible by other system parameters. Increasing the field increases the Joule heating in the channel. Excessive Joule heating generates an approximately parabolic velocity profile for the analyte ions (in the case of circular capillaries), which causes dispersion of the sample plug [19]. Grushka *et al.* [20] have derived an expression for the effective diffusion coefficient for Joule heating induced curvature of analyte profiles in cylindrical capillaries using a Taylor-Aris approach. From their model the following scaling for effective diffusivity with respect to electric field strength is obtained

$$D_{\text{eff}} = D + \frac{\Psi E^6}{D} \quad (39)$$

Where  $\Psi$  is a system-specific constant [20] associated with the viscosity of the fluid, the electrophoretic mobility of ions, buffer concentration, equivalent conductance, radius of capillary, thermal conductivity and temperature at the inner wall. From this type of relation it can be inferred that at low fields dispersion is governed by molecular diffusion and thus increasing electric field improves both *R* and *SNR*. However, at high enough fields, Joule heating induced dispersion dominates and limits the resolution and maximum peak intensities achievable, and thus there is an optimum electric field for separations. The separations should therefore be carried out at or below the optimum field, which in turn can be estimated from models such as Eq. (39) or measured experimentally.

The design methodology, which follows from these arguments, is simple. We can describe the design process as specifying the two parameters,  $h'$  and  $L'_d$ , while achieving the highest value of  $Pe_{\sigma_D}$ , limited by Joule heating.  $h'$  and  $L'_d$  must be chosen to satisfy the desired *SNR* and *R* requirement for a satisfactory separation. This is easily calculated because Eqs. (36) and (37) for *R* and *SNR*, respectively, can be solved simultaneously for the two unknown parameters  $h'$  and  $L'_d$  for a fixed  $Pe_{\sigma_D}$ . Figure 7 shows a representative plot for estimating critical sample plug length and length to the detector, assuming that the chosen value of  $Pe_{\sigma_D}$  does not cause additional, unaccounted for dispersion (e.g., due to Joule heating). Note that, if the successful separation is defined in terms of inequalities as stated in Eq. (6), then a feasible region can be defined in the parameter space. The region of

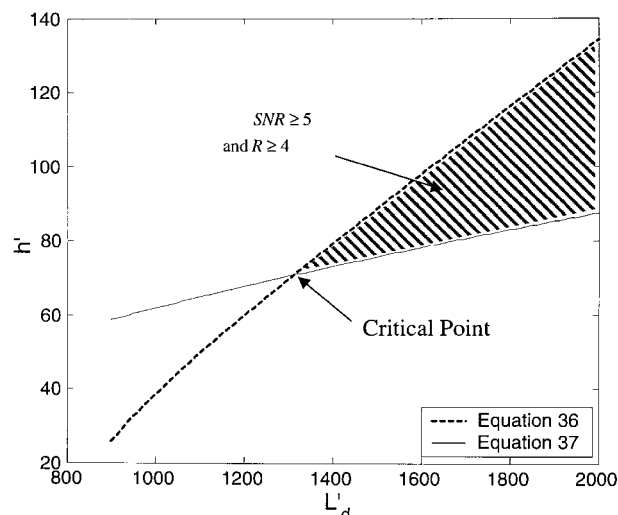


**Figure 7.** Graphical solution of Eqs. (36) and (37) describing  $R$  and  $SNR$  respectively, to obtain the feasible region in the dimensionless sample injection length and detector location parameter space for  $SNR_c = 5$  and  $R_c = 4$ . This example was calculated using  $I_0/N = 6$ ,  $\alpha = 0.2$ ,  $\beta = 0$  and  $Pe_{\sigma_D} = 1$ .

solutions satisfying the inequalities for  $R$  and  $SNR$  is shaded in Fig. 7. All choices of  $h'$  and  $L'_d$  in this region will lead to successful separations.

## 2.4 Minimization of sample injection for the high $Pe$ regime

As described earlier in the pure advection regime the  $SNR$  and  $R$  are independent of diffusive dispersion processes but are a strong function of the initial sample plug geometry and variance. Therefore, optimization of the initial injected sample plug to reduce the sample plug will enhance the separation resolution. Pure advection regimes are typically valid for high electric field separations of large molecular weight molecules (very low diffusion coefficients molecules such as DNA in separation gels). Ermakov *et al.* [5] have optimized the traditional two-step sample injection process. In the present study we optimize a three-step electrokinetic injection, first proposed by Deshpande *et al.* [21], for the pure advection limit. In the three-step injection scheme the first step is a flow of sample from sample well to the sample waste well with “pinching” from buffer wells, Fig. 8. The second step is a short flow reversal from the sample waste to the sample well and lastly sample dispensing by a flow from the buffer well to the buffer waste well with a “pull back” (minor secondary flow) into the sample and sample waste wells. The main advantage of the three-step process is that sample injection plugs with minimal advective dispersion can be generated.

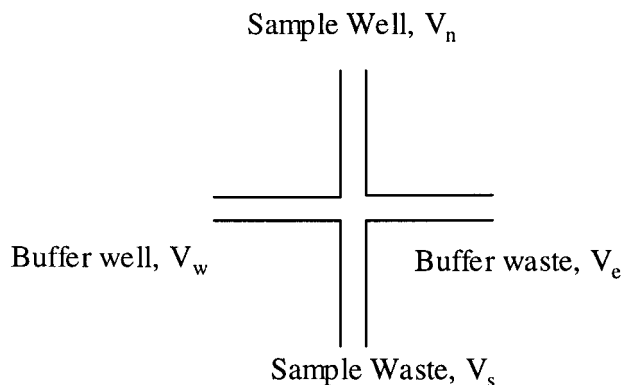


**Figure 8.** Schematic of the microchip used for performing optimization studies for low variance sample plug injections applicable to the high Peclet number limit of separation. Channel lengths in the simulation are set equal to unity.

### 2.4.1 Numerical model

In our simulation approach we assume a mathematical similarity between electroosmotic streamlines and electric field lines. The conditions for this similarity to hold have been discussed in detail by Santiago [22] and Cummings *et al.* [23]. We here applied a numerical solver developed by one of us (Mohammadi [24]), which exploits this similarity. The flow state solver for this model simulates a two-dimensional flow field. The solver neglects diffusion fluxes in the species conservation equation for the sample ions, which is consistent with the pure advection regime. In the optimization scheme the cost function to be minimized is the curvature of the injected sample plug. To minimize the injection plug variance, the electric field distribution for the first two steps was fixed arbitrarily. For the third step the ratio  $V_r/V_w$  was varied with  $V_e/V_w$  fixed to minimize the sample plug dispersion. The optimized plug curvature was then found to be a weak function of the arbitrarily determined first two steps of the simulation. Details of the algorithm and optimization scheme are described in [25]. For simplicity, we considered the case where voltage switching occurred in a time scale smaller than the advective and diffusive time scales of the problem (*i.e.*, in the simulation, voltages are switched on and off instantaneously). The electric field ratios for optimized sample plug injection are summarized in Table 1. In Fig. 9-(i), predicted analyte concentration fields for the three steps of the optimized injection process are shown.

### 2.5 Experimental setup

An inverted epifluorescence microscope (Olympus IX70) equipped with a  $10\times$  objective (Olympus, NA = 0.4) was used for imaging the concentration fields of a fluorescent

**Table 1.** Electric field scheme for optimized sample injection

Injection steps	Duration <sup>a)</sup> (s)	$E_r/E_s$	$E_e/E_s$	$E_w/E_s$
Pinching step	20	0.42	0.29	0.29
Flow reversal step	0.2	2.32	0.66	0.66
Dispensing step	5	1.00	0.43	2.43

a) For the experiments

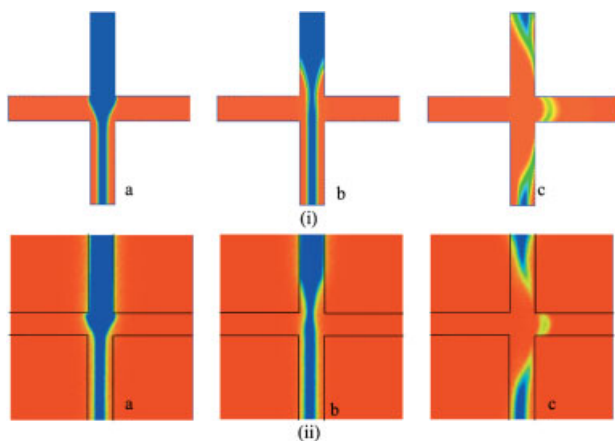


**Figure 9.** (i) Optimization results for sample injection. The false-color scale is proportional to intensity where blue is pure sample and red is background buffer. The three-step injection process as predicted using the optimized voltage scheme is shown. The voltage scheme is summarized in Table 2. In step a, sample is electrokinetically driven from sample well into the cross region with “pinching” from side channels. In step b, for a short time (such that the displacement is approximately equal to the width of the channel) the flow is reversed from the sample waste to the sample well. The narrow sample band is clear from the simulations. In step c, buffer is driven from left to right with “pull back” into the sample well and sample waste wells resulting in the injection of a narrow sample plug. In the simulation no diffusive fluxes are present, however, numerical diffusion imparts some dispersion. (ii) Experimental validation of optimized voltage scheme for injecting of low variance sample plugs with minimal curvature. Normalized CCD epifluorescent images for an optimized sample injection for a high molecular weight, low diffusivity fluorescein-dextran dye is shown. The channel boundaries have been added for clarity. The duration of the various steps are listed in Table 1.

dye mixture. Illumination from a mercury lamp was spectrally filtered at the peak fluorescein absorption and emission wavelengths of 485 nm and 535 nm, respectively. Images were captured using an intensified CCD camera (I-PentaMAX, Gen III, Princeton Instruments) with a 512 × 512 CCD pixel array and 12-bit digitization. The expo-

sure time was 2 ms and the frame rate was 15 frames per second. A low fluorescence Borofloat glass microchip (Micalyne, Alberta, Canada) with a single channel intersection (*i.e.*, a cross-type injection scheme) was used for all experiments. The microchannel width is 50 μm and their centerline depth is 20 μm. The channels have the characteristic shape of an isotropic wet etch. The length of the vertical channel is 8 mm and the length of the horizontal channel is 85 mm. A high voltage power supply (Micalyne, Alberta, Canada, 6 kV maximum) was used to control platinum electrode potentials mated to the four chip reservoirs. In the separation experiments, we used a 10 mM borate buffer prepared by dissolving borax in deionized water. The sample was a mixture of 80 μM sodium fluorescein dye (sodium salt of fluorescein, Baker) and 155 μM Bodipy dye (Molecular Probes, Eugene, OR, USA) in 10 mM borate buffer. In experimental validations of the optimal injection voltage scheme, we used a 47 μM solution of low diffusivity fluorescein-dextran conjugate (approximate molecular mass 70 kDa) dissolved in 10 mM borate buffer was used.

### 2.5.1 Image analysis

CCD images were corrected by applying the following matrix operation to each image:

$$I_{\text{corr}} = \frac{I_{\text{raw}} - I_{\text{background}}}{I_{\text{flatfield}} - I_{\text{background}}} \quad (40)$$

In this approach for quantitative imaging, a background image is subtracted from the raw image and this difference is normalized by the difference between a flatfield and the background image. The flatfield image was obtained by imaging of the microchannels filled with a homogeneous concentration of dye. To compare the two dimensional image data with the one-dimensional model, the intensity data for the pixel regions of the microchannel images were averaged along the vertical direction (*i.e.*, the width of the microchannel) to get one-dimensional axial intensity profiles. This operation results in an increase in *SNR* of the detected axial distribution signal.

## 3 Results and discussion

### 3.1 Calibration of electrokinetic injections

To provide a meaningful comparison to our model, we used the one-dimensional intensity profiles described above to determine the *SNR* and *R* of the experiments. In these experiments, the shape and intensity of the injected sample plugs is difficult to predict analytically because of electrophoretic biasing of the injected species

[26], and advective and diffusive dispersion resulting from the injection process. Note that electrophoretic biasing is a function of the voltage schemes applied and the mobility of the dyes, and in general difficult for chip designers to predict. Therefore, in order to validate our model, we chose an approach where we empirically determine the peak intensity and variance of individually injected sample species in a set of preliminary calibration experiments. This calibration step also provided estimates of the mobilities and diffusivities of the fluorescein and bodipy dyes. The injection scheme used was a more traditional two-step process of sample pinching and sample dispensing [5]. These initial calibrations which injected first only fluorescein and then only bodipy provided data which is analogous to the type of information which a separation system designer would need in order to accurately predict optimal separation conditions.

The initial sample plug calibrations discussed above resulted in one-dimensional concentration profiles, which were very closely Gaussian. Figure 10 shows typical vertical averaged axial intensity data from the calibration experiments with fitted Gaussian curves. The excellent fit between the experimental profiles and the characteristic Gaussian peak development suggest that the diffusive dispersion model incorporated in to the model above is valid. The maximum injected sample peak is around only 40% of the intensity corresponding to the concentration in the sample well. This is indicative of the effects of diffusion during the pull back step and due to the dispersion of sample plug associated with the curved equipotential lines in the region of the channel intersection.

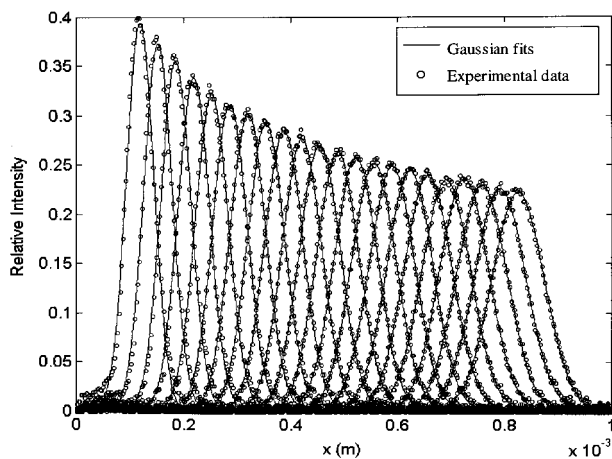


**Figure 10.** Calibration of fluorescein electrokinetic injection at field strength of 200 V/cm. The two-dimensional intensity distributions from the CCD images are vertically averaged along the channel width to generate a one-dimensional data. Gaussian curves are fit to the experimental data to measure diffusion coefficients, mobilities and initial injection parameters. Time between each plot is 67 ms.

The diffusivity of the sample analytes is a strong function of temperature and, therefore, applied electric field for any given separation. We therefore measured diffusivity for each analyte within our microchannel system for each of the electric field intensities of interest. These data are shown in Table 2. These values were obtained by fitting all of the temporally developing data (*i.e.*, the profile at all times) using a single diffusivity value, and this process was repeated for each field intensity. The measured fluorescein diffusivity at the lowest field (which should be very near room temperature) compares well with published values of  $4.4 \times 10^{-10} \text{ m}^2/\text{s}$  [27] and  $6.4 \times 10^{-10} \text{ m}^2/\text{s}$  [28]. This suggests that our system has negligible value of dispersive velocity  $U_d$ .

**Table 2.** Measured diffusion coefficient as a function of electric field intensity

$E$ (V/cm)	Diffusion coefficient ( $\times 10^{10} \text{ m}^2/\text{s}$ )	
	Fluorescein	Bodipy
50	5.1	6.2
100	5.2	6.3
200	5.4	6.6

The effective mobilities (*i.e.*, the arithmetic sum of the sample electrophoretic mobility and the electroosmotic mobility of the channel) were measured to be  $2.4 \times 10^{-4} \text{ cm}^2/\text{Vs}$  and  $3.4 \times 10^{-4} \text{ cm}^2/\text{Vs}$  for fluorescein and Bodipy, respectively. Gaussian fits of the data immediately after the completion of the injection, provided a characterization of the initial injected sample plug in terms of peak intensity, location, and spatial variance for three separation electric fields: 50, 100 and 200 V/cm.

### 3.2 Validation of SNR and $R$ model

In the separation experiments, the sample concentrations were chosen to provide an SNR high enough to yield accurate measures of peak height and resolution. Figure 11-(i) shows a typical experimental data for the separation experiment of fluorescein and Bodipy. Twenty curves of this data are plotted to show the extent of data made possible by full-field detection with a CCD camera. This type of data yields a more comprehensive validation of electromigration/convective/diffusion models of separations as compared to data from single point detections. The individual peak intensities and the resolution were extracted from the experimental profiles by simply fitting the data with the sum of two Gaussians.

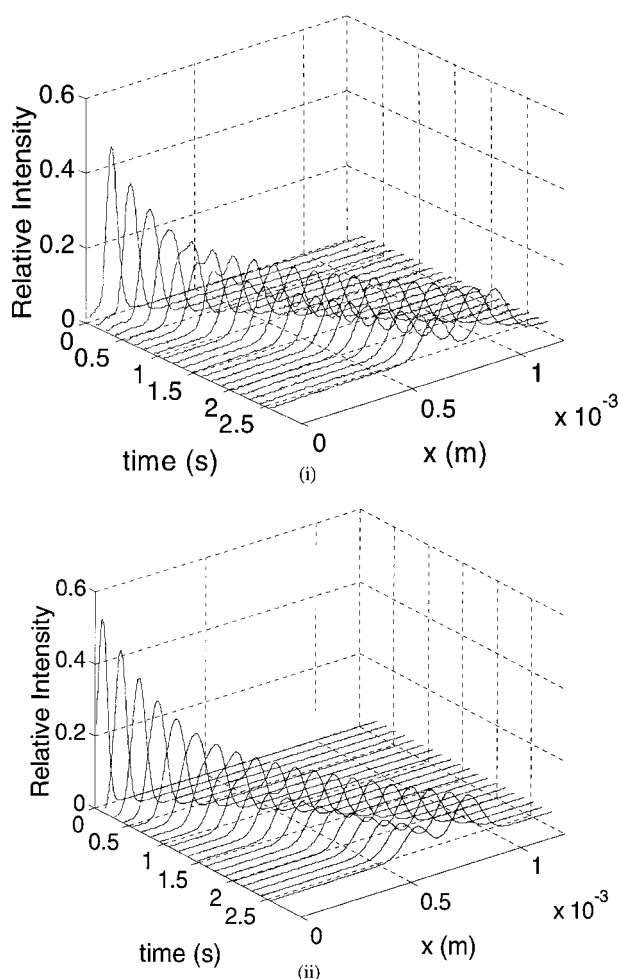


**Figure 11.** (i) Full-field detection of axial intensity profiles for the electrophoretic separation of fluorescein and Bodipy using a CCD array. Using this mode of detection both spatial and temporal distribution can be measured with high resolution. The applied field is  $E = 100$  V/cm. Time between individual plots is 67 ms. An initial unimodal sample plug develops into a bimodal profile of lower intensity as the analytes separate and diffuse. (ii) Model predictions for separation of fluorescein and bodipy based on the CCD detector output model Eq. (22). The parameters required for the model are diffusion coefficient, mobilities and initial sample plug characteristics. These parameters were predicted using independent measurements of individual dye experiments.

Our model for the separation of two dyes is based on summation of individual dye intensities of the form given by Eq. (22). The calibration measurements of the initial peak intensity, location, and spatial variance performed on the individually injected dye samples were used to predict the initial condition of the separation model. The model was then used to predict the development of the axial concentration fields throughout the separation. To

compare the model with mixed dye experiment, following scaling with respect to flatfield images was used for the individual dye initial peak intensity data measured in calibration step

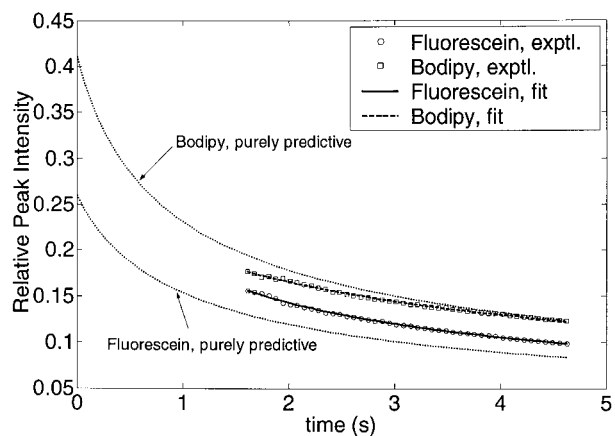
$$I_{\text{corr,FI}} = \left( \frac{I_{\text{raw,FI}} - I_{\text{background,FI}}}{I_{\text{flatfield,Mix}} - I_{\text{background,Mix}}} \right) \quad (41)$$

Here  $I_{\text{flatfield,Mix}}$  refers to the measured flatfield image obtained by filling the channel with the two-dye solution, subscript FI refers to visualizations performed on fluorescein alone. Similar scaling was used for Bodipy injection calibration data. In this way, the model curves we can generate are purely predictive and based on: (i) two single-species, empirically-determined initial conditions which predict the initial condition expected in the separation experiment, and (ii) the advective diffusion model described earlier. The model predictions for the temporal and spatial concentration distribution are shown in Fig. 11-(i) and suggest a good agreement with the experimental data.

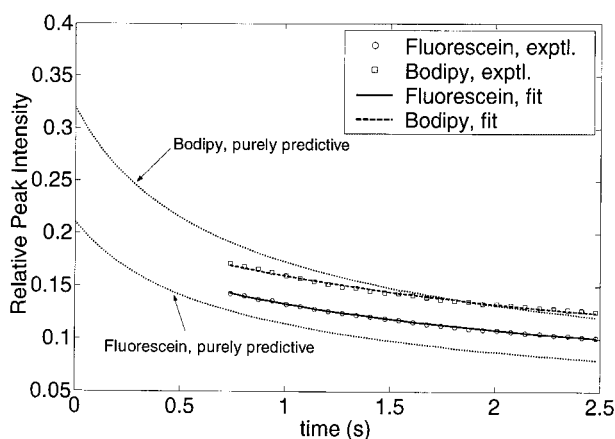
Figure 12 shows the comparison between experimentally determined peak intensities of each dye and model predictions. We present both model predictions based solely on calibration experiments as well as nonlinear least squares fits to the experimental data of the form given by the following relation for peak intensity, derived from Eq. (22):

$$I_{\text{CCD}}(t) = \frac{I_0}{\sqrt{2\pi(\sigma_0^2 + 2D_{\text{eff}}t)}} \quad (42)$$

The fitting parameters in the least-squares calculations are  $I_0$  and the initial sample plug variance  $\sigma_0$ . The experimental data for individual peak heights is plotted only for those times for which the resolution is high enough to accurately discern the two sample peaks. The trends of the data are very accurately captured by the model and the absolute values of intensities compare fairly well. The discrepancies between the absolute values of the model and predicted intensities are probably due to photobleaching of dyes, temperature dependence of fluorescence, electrophoretic bias of the electrokinetic injections and due to slight differences in illumination (e.g., because of drift of the mercury bulb intensity). Figure 13 compares the model predictions and experimentally measured resolution between the two dyes. Again, the model compares well with the data. Together, Figs. 11, 12, and 13 show that predictions made from independent observations of species in a well-characterized system, can be used to accurately predict the dynamics of a separation and can be used to design for an optimal injection length for a given length to detector and detector width.



(a)



(b)

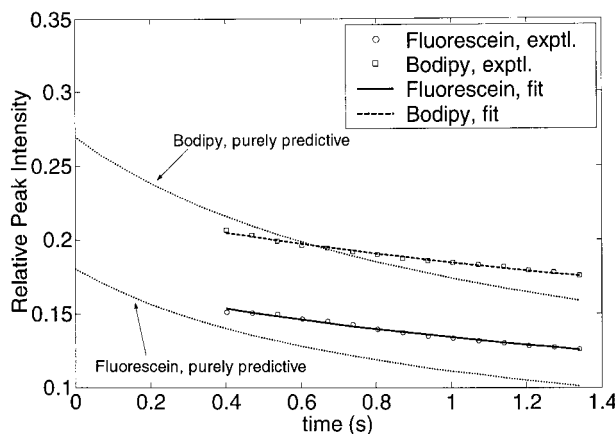


**Figure 12.** Comparison of model prediction of peak heights for each dye and experimental data. Experimental peak heights are plotted for each analyte at downstream locations of the analyte bands where the resolution,  $R$ , is approximately greater than 2. Also shown are simple fits to the experimental data based on Eq. (22) using  $I_0$  and  $\sigma_0$  as fitting parameters. The predictions are calculated based on electrophoretic mobility and diffusivity values determined from independent experiments in the same experimental setup. Plots (a), (b), (c) are for separation fields of 50, 100 and 200 V/cm respectively.

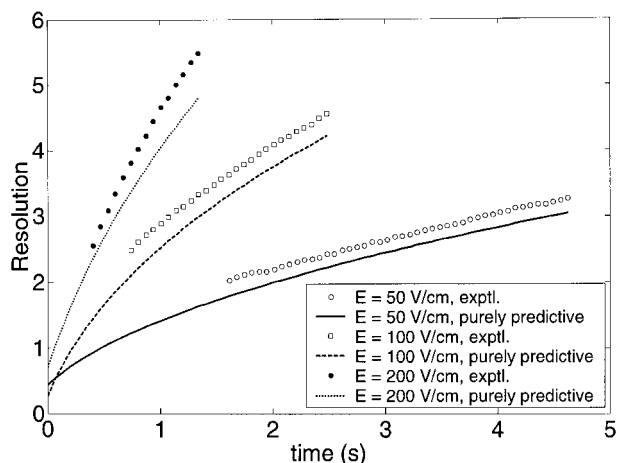


**Figure 13.** Comparison of predicted and experimentally observed separation resolution. Symbols correspond to experimental data. As shown by Eq. (36), electric field (through parameter  $Pe_{\sigma_D}$ ) has a strong effect on the time rate of change of resolution.

### 3.3 Validation of minimal variance injection scheme

Next, we performed a set of experiments to validate the minimal injection dispersion scheme discussed earlier. Again, this scheme is applicable to high Peclet limit separations with adequate SNR where controlling the shape of the injection sample plug is critical. Figure 9-(ii) shows instantaneous images of the injection process. The images can be compared with those predicted by the simulation which are shown in Fig. 9-(i). Experimental concentration profiles compare fairly well with the simulation profiles. There are slight discrepancies in the shape and concentration of the profiles. Two reasons for this are the effects of finite voltage switching times and finite diffusivity in the experiment despite the use of a low diffusivity dye. The effects of voltage transients are especially important throughout the second step in the injection protocol because the flow reversal is performed for a very short time (approximately 0.2 s). The dispersion associated with the narrow sample injection leads to an 80% decrease in the injected sample intensity as compared to the concentration in the sample well. We therefore again see that such a minimal variance injection scheme will be useful only for cases that are not SNR limited. The injected sample width, defined as the standard deviation of the plug, was approximately 10  $\mu\text{m}$  or around one fifth of the channel width.

Lastly, it is interesting to note the scaling of  $R$  with respect to injection lengths for the injection-variance-limited case

$$R|_{h\text{-limited}} \cong \frac{\alpha L'_d \sqrt{3}}{(1 + \beta)h} \quad (43)$$

This relation shows that resolution scales approximately as  $1/h'$  (e.g., if the injection width is halved, the resolution is doubled). This suggests that microchip area can be reduced by a factor of two by using optimized injections for a given desired resolution.

#### 4 Concluding remarks

The validity of an electrophoretic separation can be characterized in terms of two parameters: separation resolution, which refers to the ability to discriminate the two most closely spaced peaks; and the signal-to-noise ratio, which refers to the certainty with which the signal can be differentiated from background noise. We have developed a model for detector output from CCD arrays and point-wise detectors (modeled as either a Gaussian aperture or Boxcar aperture) using Taylor dispersion Eq. for the ion concentration in the channel. Using this model,  $SNR$  and  $R$  can be related to the concentration distribution in electrophoretic separations. Nondimensionalization yields three important parameters  $h'$ ,  $L'_d$ , and  $Pe_{\sigma_D}$ . Several tradeoffs exist with respect to the first two parameters but both  $SNR$  and  $R$  increase with Peclet number. Using these expressions for  $SNR$  and  $R$ , optimum values for injection lengths and length-to-detector can be calculated which allows the experimentalist to choose between, for example, simple cross and staggered-T CE microchips. If a gated, cross-microchannel injection approach is used, the experimentalist can choose among a wide range of injection lengths to custom tailor the separation. For the high  $Pe$  limit case where  $SNR$  is not a concern, we have used simulation and optimization tools to design minimal variance injections for simple cross-chip systems. The standard deviation of the optimized sample plug was measured to be less than 10  $\mu\text{m}$  (one-fifth of the channel width). Given well-designed, sensitive detectors, such narrow sample bands offer a way of reducing analysis time, microchip length scales, and on-chip voltage levels.

Optimized on-chip electrophoretic separations are essential to realizing the potential of miniaturized separation systems in terms of high throughput and automation. To this end, a set of unambiguous performance measures and figures of merit are essential. Ideally, such quantitative descriptions of system performance can be combined with state-of-the-art methods of sample preconcentration (e.g., sample stacking to increase  $SNR$ ), reduction of sample dispersion in a variety of electrokinetic flow geometries [7], and improvements in detection modalities to evolve the design and efficacy of electrokinetic microchips.

The authors gratefully acknowledge the support of the Defense Advanced Research Projects Agency contract number F30602-00-2-0609 with Dr. Anantha Krishnan as monitor.

Received December 1, 2001

#### 5 References

- [1] Dolnik, V., Liu, S., Jovanovich, S., *Electrophoresis* 2000, 21, 41–54.
- [2] Harrison, D. J., Fluri, K., Seiler, K., Fan, Z., Effenhauser, C. S., Manz, A., *Science* 1993, 261, 895–897.
- [3] Giddings, J. C., *Unified Separation Science*, Wiley-Interscience, New York 1991, 96–109.
- [4] Bier, M., Palusinski, O. A., Mosher, R. A., Saville, D. A., *Science* 1983, 219, 1281–1287.
- [5] Ermakov, S. V., Jacobson, S. C., Ramsey, J. M., *Anal. Chem.* 2000, 72, 3512–3517.
- [6] Patankar, N. A., Howard, H. H., *Anal. Chem.* 1998, 70, 1870–1881.
- [7] Molho, J. I., Herr, A. E., Mosier, B. P., Santiago, J. G., Kenny, T. W., *Anal. Chem.* 2001, 73, 1350–1360.
- [8] Gaš, B., Stedry, M., Kenndler, E., *Electrophoresis* 1997, 18, 2123–2133.
- [9] Catsimopoulos, N., *Isoelectric Focusing*, Academic Press, San Francisco, CA 1976, 93–118.
- [10] McCabe, L. W., Smith, J. C., Harriott, P., *Unit Operations of Chemical Engineering*, McGraw-Hill Book Co., Singapore 1993, 521–587.
- [11] Giddings, J. C., *Unified Separation Science*, Wiley-Interscience, New York 1991, 97–98.
- [12] Probstein, R. F., *Physicochemical Hydrodynamics: An Introduction*, 2<sup>nd</sup> ed., John Wiley & Sons, New York, 82–96.
- [13] Aris, R., *Proc. R. Soc. London, Ser. A* 1956, 235, 67–77.
- [14] Taylor, G. I., *Proc. R. Soc. London, Ser. A* 1953, 219, 186–203.
- [15] Dutta, D., Leighton, D. T., *Anal. Chem.* 2001, 73, 504–513.
- [16] Anderson, J. L., Idol, W. K., *Chem. Eng. Commun.* 1985, 38, 93–106.
- [17] Ghosal, S., *Anal. Chem.* 2002, 74, 771–775.
- [18] Khaledi, M. G., *High-Performance Capillary Electrophoresis*, John Wiley & Sons, Inc., New York 1998, 146, 303–401.
- [19] Gobie, W. A., Ivory, C. F., *J. Chromatogr.* 1990, 516, 191–210.
- [20] Grushka, E., McCormick, R. M., Kirkland, J. J., *Anal. Chem.* 1989, 61, 241–246.
- [21] Deshpande, M., Greinner, K. B., West, J., Gilbert, J. R., Bousse, L., Minalla, A., *Micro Total Analysis Systems*, Kluwer Academic Publishers, The Netherlands 2000, 339–342.
- [22] Santiago, J. G., *Anal. Chem.* 2001, 73, 2535–2365.
- [23] Cummings, E. B., Griffiths, S. K., Nilson, R. H., Paul, P. H., *Anal. Chem.* 2000, 72, 2526–2532.
- [24] Mohammadi, B., *Int. J. Numer. Methods Fluids* 1997, 25, 183–203.
- [25] Mohammadi, B., Santiago, J. G., *ESAIM-Math. Model. Num.* 2001, 35, 513–523.
- [26] Alarie, J. P., Jacobson, S. C., Ramsey, J. M., *Electrophoresis* 2001, 22, 312–317.
- [27] Paul, P. H., Garguilo, M. G., Rakestraw D. J., *Anal. Chem.* 1998, 70, 2459–2467.
- [28] Furukawa, R., Arauz-Lara, J. L., Ware, B. R., *Macromolecules* 1991, 24, 599–605.

## Appendix A

Here we summarize the expected detector output signals for the boxcar apertured point-wise detector described in Section 2.1.2.2.

### (i) Boxcar aperture detection of a Gaussian injection

The resulting signal from an initially Gaussian sample plug detected by a boxcar aperture can be determined by evaluating the integral in Eq. (28) to derive

$$I(t) = \frac{I_0}{2} \left( \operatorname{erf} \left( \frac{\delta - L_d + Ut}{\sqrt{2}\sigma'} \right) + \operatorname{erf} \left( \frac{\delta + L_d - Ut}{\sqrt{2}\sigma'} \right) \right) \quad (\text{A-1})$$

where,

$$I_0 = D_0 C_0$$

$$\bar{\sigma}^2 = \sigma_0^2 + 2D_{\text{eff}}t$$

Note the dependence of the signal on the various lengths scales described in Fig. 1.

### (ii) Boxcar aperture detection of a boxcar injection

Similarly, the convolution of the analyte bands resulting from a boxcar-type injection of sample with a boxcar aperture detector is

$$I(t) = \frac{D_0 C_0}{\sqrt{2\pi}\sigma} \int_{-\infty}^{\infty} \int_{-h}^h \exp \left( -\frac{(x - Ut - y)^2}{2\sigma^2} \right) dy dx = \frac{I_0}{\sqrt{\pi}} (I_1 - I_2) \quad (\text{A-2})$$

where

$$I_0 = D_0 C_0$$

$$I_1(t) = (b - \lambda) \operatorname{erf} \left( \frac{b - \lambda}{\sqrt{2}\sigma} \right) - (a - \lambda) \operatorname{erf} \left( \frac{a - \lambda}{\sqrt{2}\sigma} \right) + \sqrt{\frac{2}{\pi}} \sigma \left[ \exp \left( -\left( \frac{b - \lambda}{\sqrt{2}\sigma} \right)^2 \right) - \exp \left( -\left( \frac{a - \lambda}{\sqrt{2}\sigma} \right)^2 \right) \right]$$

$$I_2(t) = (b - \beta) \operatorname{erf} \left( \frac{b - \beta}{\sqrt{2}\sigma} \right) - (a - \lambda) \operatorname{erf} \left( \frac{a - \beta}{\sqrt{2}\sigma} \right) + \sqrt{\frac{2}{\pi}} \sigma \left[ \exp \left( -\left( \frac{b - \beta}{\sqrt{2}\sigma} \right)^2 \right) - \exp \left( -\left( \frac{a - \beta}{\sqrt{2}\sigma} \right)^2 \right) \right]$$

$$a = L_D - \delta$$

$$b = L_D - \delta$$

$$\sigma = \sqrt{2D_{\text{eff}}t}$$

$$\lambda = Ut - h$$

$$\beta = Ut + h$$